Giant tunneling magnetoresistance induced by bias voltage in spin-filter van der Waals magnetic tunnel junctions with an interlayer antiferromagnetic semiconductor barrier

Xiaoyan Guo,[1] Baishun Yang,[2] Xiaolin Zhang,[1] Yu Zhu,[1,3] Xiufeng Han,[3] and Yu Yan[1,*]

[1]*Key Laboratory of Physics and Technology for Advanced Batteries (Ministry of Education), Department of Physics, Jilin University, Changchun 130012, China*

[2]*Shenzhen JL Computational Science and Applied Research Institute, Shenzhen 518109, China*

[3]*Beijing National Laboratory for Condensed Matter Physics, Institute of Physics, University of Chinese Academy of Sciences, Chinese Academy of Sciences, Beijing 100190, China*

(Received 13 May 2021; revised 11 September 2021; accepted 11 October 2021; published 25 October 2021)

Spin-filter van der Waals Magnetic tunnel junctions (sf-vdW MTJs) formed by an interlayer antiferromagnetic (AFM) vdW semiconductor as a barrier have exhibited promising prospects in achieving a high tunneling magnetoresistance (TMR) ratio in MTJs. Here, using first-principles calculations, we investigate the spin-dependent transport and the TMR effect of sf-vdW MTJs formed by sandwiching bilayer and trilayer $NiBr_2$ barriers between two graphite electrodes ($Gr/NiBr_2/Gr$ sf-vdW MTJs). Similar to the experimental results of sf-vdW MTJs formed by a few-layer CrI_3 barrier, the TMR ratios of the $Gr/NiBr_2/Gr$ sf-vdW MTJs increase first with the increase of bias voltage and decrease with the further increase of bias voltage after reaching the highest points because the conduction bands of the interlayer ferromagnetic (FM) $NiBr_2$ barrier at the K points go into the bias window earlier than those of the interlayer AFM $NiBr_2$ barrier with the increase of bias voltage. Compared to the TMR ratios of about 170% and 206% at zero bias voltage, the TMR ratios of the $Gr/NiBr_2/Gr$ sf-vdW MTJs with bilayer and trilayer $NiBr_2$ barriers are largely increased about 34 and 67 times by the optimized bias voltage, respectively. Correspondingly, a giant TMR ratio of about 6000% and 14 000% can be achieved in the $Gr/NiBr_2/Gr$ sf-vdW MTJs with bilayer and trilayer $NiBr_2$ barriers at 0.14 and 0.125 V bias voltage, respectively. Our results elucidate the mechanism of bias voltage induced giant TMR ratio in the $Gr/NiBr_2/Gr$ sf-vdW MTJs and provide promising routes for developing MTJs with a high TMR ratio.

DOI: 10.1103/PhysRevB.104.144423

I. INTRODUCTION

Magnetic tunnel junctions (MTJs) are the subject of an intensive research recently due to their potential applications in spintronics, and the high tunneling magnetoresistance (TMR) ratio is the key functional property of MTJs to develop high-performance spintronic devices [1–3]. To achieve a high TMR ratio in MTJs, tremendous efforts have been made over the past two decades [4–12]. The experimental discovery of van der Waals (vdW) intrinsic magnets offers an intriguing approach to design high-performance vdW MTJs [13–26]. In particular, spin-filter vdW MTJs (sf-vdW MTJs) formed by the interlayer antiferromagnetic (AFM) vdW semiconductor as barrier have exhibited inspiring prospects in achieving a high TMR ratio in MTJs [22–34]. For example, using an external magnetic field to change the interlayer ordering of few-layer CrI_3 from AFM to ferromagnetic (FM), a high TMR ratio of 95%, 300%, and 550% was experimentally achieved in sf-vdW MTJs based on graphite/CrI_3/graphite heterostructures with bilayer, trilayer, and tetralayer CrI_3 barriers at zero bias voltage, respectively [22]. More importantly, it was experimentally reported that at the optimized biasing voltage, a giant TMR ratio of up to 10 000%, 19 000% and 1 000 000% can be achieved in sf-vdW MTJs based on graphite/CrI_3/graphite vdW heterostructures with CrI_3 barriers of different thicknesses at low temperature under an applied magnetic field, respectively [26–28], and the TMR ratio of sf-vdW MTJs formed by sandwiching tetralayer CrI_3 between graphene contacts can be continuously modulated from 17 000% to 57 000% by back gate voltage [25]. These experimental results reveal that switching of the interlayer coupling of two-dimensional (2D) vdW magnetic semiconductor and the optimized biasing voltage are of vital importance for achieving a giant TMR ratio in sf-vdW MTJs formed by the interlayer AFM vdW semiconductor as barrier. Theoretically, using first-principles calculations, Heath *et al.* found that the interlayer coupling of the CrI_3 barrier is key to properly describing electronic properties and spin-dependent transport in sf-vdW MTJs based on trilayer graphene/few-layer CrI_3/trilayer graphene heterostructures, in which few-layer CrI_3 in the rhombohedral (low-temperature) phase was used as a barrier of sf-vdW MTJs [31]. It was theoretically reported that the interlayer coupling of few-layer CrI_3 in the low-temperature phase are FM, while the weak interlayer AFM state exists in a few-layer CrI_3 with monoclinic (high-temperature) phase [35,36]. Correspondingly, it has been experimentally demonstrated that the interlayer magnetic coupling in few-layer CrI_3 is AFM [22,26,37]. As known, the TMR effect of sf-vdW MTJ comes from the change in resistance when the magnetism of the barrier switches between AFM and FM states. Therefore, to

*yanyu@jlu.edu.cn

deeply understand the bias voltage induced giant TMR ratio, it may be necessary to use the layered magnetic material with a considerable interlayer magnetic coupling as a magnetic barrier to theoretically investigate the influence of interlayer coupling switching of the vdW magnetic barrier on spin-dependent transport and giant TMR ratio in sf-vdW MTJs at bias voltage by properly describing switching of the interlayer coupling of the vdW magnetic barrier. More notable is that CrI_3 turns into a liquid within minutes in ambient conditions [38,39] and only BN-encapsulated CrI_3 is stable and can be used in electronic devices, which make CrI_3 investigation and integration into spintronic devices more complicated. It is therefore desirable to explore new vdW magnetic materials with a higher ambient stability to make it more convenient to integrate vdW magnetic materials into spintronic devices.

Except for the metal trihalides represented by CrI_3, layered metal dihalides are also a family of vdW intrinsically magnetic materials [40–43]. Among metal dihalides, bulk $NiBr_2$ with the rhombohedral $CdCl_2$ structure was demonstrated to be a vdW intrinsically magnetic semiconductor with magnetic structure of intralayer FM and interlayer AFM orderings [44–48]. Furthermore, it was experimentally reported that the Néel temperature of bulk $NiBr_2$ is about 52 K and the magnetic easy axis is in-plane [44]. It is worth noting that the calculated formation energy of $NiBr_2$ is -1.50 eV/atom [41], which is much smaller than those of both rhombohedral and monoclinic phases of CrI_3 [49], thus $NiBr_2$ is more energetically stable. Moreover, the calculated exfoliation energies of $NiBr_2$ and NiI_2 are smaller than that of graphite, indicating the easy preparation of monolayer and few-layer $NiBr_2$ and NiI_2 [48]. Experimentally, the monolayer and few-layer NiI_2 flakes were epitaxially grown on *h*-BN and few-layer NiI_2 was partly hydrating within 2 hours in air [50], in contrast to the irreversible degradation of CrI_3 within seconds in ambient conditions. Therefore, not only few-layer $NiBr_2$ may be prepared in the future but may not degrade rapidly under ambient conditions, as well as a high TMR ratio may be achieved in sf-vdW MTJs formed by few-layer $NiBr_2$ as barrier at the optimized biasing voltage.

Here, we design sf-vdW MTJs formed by sandwiching bilayer and trilayer $NiBr_2$ barriers between two graphite electrodes ($Gr/NiBr_2/Gr$ sf-vdW MTJs), and investigate the spin-dependent transport and the TMR effect of the $Gr/NiBr_2/Gr$ sf-vdW MTJs using first-principles calculations. Similar to the experimental results of sf-vdW MTJs formed by a few-layer CrI_3 barrier [25–27], the TMR ratios of the $Gr/NiBr_2/Gr$ sf-vdW MTJs increase first with the increase of bias voltage and decrease with the further increase of bias voltage after reaching the highest points. In particular, a giant TMR ratio of about 6000% and 14 000% can be achieved in the $Gr/NiBr_2/Gr$ sf-vdW MTJs with bilayer and trilayer $NiBr_2$ barriers at the optimized biasing voltage, respectively.

II. COMPUTATIONAL METHODS

First-principles calculations for structure optimization, bader charge, work function, and magnetism are performed using density functional theory (DFT) within the projector augmented wave method as implemented in the Vienna *ab initio* Simulation Package (VASP) [51–54]. The exchange-correlation functional is approximated by the generalized gradient approximation (GGA) of the Perdew-Burke-Ernzerhof version [55], and the interlayer vdW interactions are taken into account by the optB86b-vdW exchange functional [56]. The energy cutoff of the plane wave expansion is set to be 500 eV, and the convergence criteria for energy and force are set to be 1×10^{-6} eV and 0.01 eV/Å, respectively. A vacuum space of more than 15 Å is used to avoid the spurious interaction between periodic replicas, and a Γ-centered *k* mesh of $11 \times 11 \times 1$ is used to sample the first Brillouin zone (BZ) of monolayer, bilayer, and trilayer $NiBr_2$ as well as three-layers graphene/$NiBr_2$/three-layers graphene ($Gr/NiBr_2/Gr$) heterostructure.

The calculations for electronic structure and quantum transport are performed using the NANODCAL package based on real-space DFT combined with the Keldysh nonequilibrium Green's function formalism [57]. $7 \times 7 \times 1$ and $150 \times 150 \times 1$ Monkhorst–Pack *k* points are used for self-consistent calculations and calculating conductance and current, respectively. At zero bias voltage, the spin-resolved conductance of sf-vdW MTJs is calculated by

$$G_\sigma = \frac{e^2}{h} \sum_{k_\parallel} T_\sigma(k_\parallel, E_F), \tag{1}$$

where T_σ $(E_F, k_\parallel)$ is the transmission coefficient with spin σ ($\sigma = \uparrow, \downarrow$) at the Fermi level E_F and transverse Bloch wave vector $k_\parallel$, e, and h are the electron charge and the Planck constant, respectively.

The spin-resolved tunneling current of sf-vdW MTJs at a bias voltage V can be obtained by the Landauer-Buttiker formula

$$I_\sigma = \frac{e}{h} \int T_\sigma(E, V)[f_l(E - \mu_l) - f_r(E - \mu_r)]dE, \tag{2}$$

where f_l (f_r) and μ_l (μ_r) are the Fermi distribution function and the chemical potential of the left (right) electrodes, respectively.

III. RESULTS AND DISCUSSION

A. Structure of $NiBr_2$ and $Gr/NiBr_2/Gr$ sf-vdW MTJs

Bulk $NiBr_2$ adopts the rhombohedral $CdCl_2$ layered structure with the space group $R\bar{3}m$, in which the blocks of monolayer $NiBr_2$ are stacked together by weak vdW interaction along the *c* axis and the layer stacking sequence is strictly ABC. In monolayer $NiBr_2$, a honeycomb Ni layer is sandwiched between two Br layers through the Ni-Br bonds in antiprismatic coordination. The optimized structure parameters of bulk and monolayer $NiBr_2$, such as lattice constant, bond length, and the interlayer distance, are in agreement with previously calculated and measured values [40–47]. Furthermore, our calculations show that, no matter what intra and interlayer magnetic couplings are FM or AFM, the energies of AB-stacked bilayer, ABC-stacked trilayer, and ABC-stacked bulk $NiBr_2$ are slightly higher than those of AA-stacked bilayer, AAA-stacked trilayer, and AAA-stacked bulk $NiBr_2$, respectively. For instance, when the interlayer coupling is of AFM order, the energies of AB-stacked bilayer, ABC-stacked trilayer, and ABC-stacked bulk $NiBr_2$

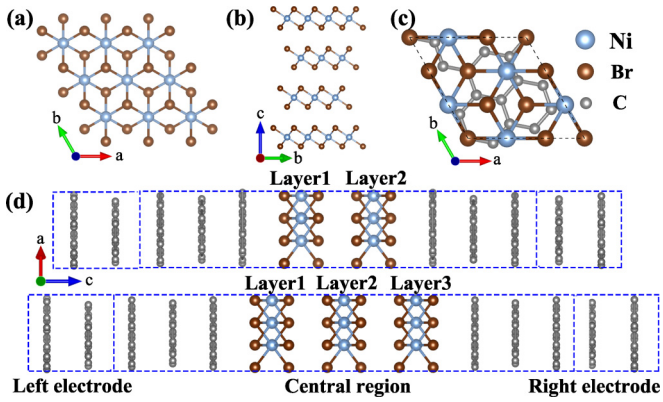

FIG. 1. (a) Top view of monolayer $NiBr_2$ and (b) side view of bulk $NiBr_2$. (c) Top view of the interface between graphene and $NiBr_2$ in the $Gr/NiBr_2/Gr$ heterostructures. (d) Side views of the $Gr/NiBr_2/Gr$ sf-vdW MTJs with bilayer and trilayer $NiBr_2$ barriers, respectively.

are 1.30, 0.75, and 1.27 meV/formula unit higher than those of AA-stacked bilayer, AAA-stacked trilayer, and AAA-stacked bulk $NiBr_2$. Referring to the experimental results of ABC stacking sequence in bulk $NiBr_2$ [43–45] and the small energy difference between the AAA-stacked (AA-stacked) sequence and ABC-stacked (AB-stacked) sequence, we construct the $Gr/NiBr_2/Gr$ sf-vdW MTJs using AB-stacked bilayer and ABC-stacked trilayer $NiBr_2$ as barriers. As shown in Fig. 1(d), the designed $Gr/NiBr_2/Gr$ sf-vdW MTJs consist of semi-infinite left and right graphite electrodes and central region, and the central region is a vdW heterostructure formed by sandwiching bilayer or trilayer $NiBr_2$ barrier between two trilayer graphene buffer layers. To reduce the lattice mismatch between the graphene and $NiBr_2$ layers at the interface, a $\sqrt{3} \times \sqrt{3}$ unit cell of $NiBr_2$ and a $\sqrt{7} \times \sqrt{7}$ unit cell of graphene are used to build trilayer graphene/bilayer (trilayer) $NiBr_2$/trilayer graphene ($Gr/NiBr_2/Gr$) vdW heterostructure and the in-plane lattice constant of the $Gr/NiBr_2/Gr$ vdW heterostructure is set as 6.407 Å, thus graphite is compressed about 1.1% and $NiBr_2$ is stretched about 0.8%. The optimized interlayer distance between interfacial graphene and $NiBr_2$ layer in the $Gr/NiBr_2/Gr$ vdW heterostructures is 3.45 Å. Herein, two (three) monolayers of the bilayer (trilayer) $NiBr_2$ barrier in the $Gr/NiBr_2/Gr$ vdW heterostructure are denoted by Layer 1 and Layer 2 (Layer 1, Layer 2, and Layer 3), respectively, as shown in Fig. 1(d).

B. Electronic structure and magnetism of $NiBr_2$ and $Gr/NiBr_2/Gr$ vdW heterostructures

Consistent with the report by the authors of Ref. [42], our calculations show that bulk $NiBr_2$ is an intrinsically magnetic semiconductor with the magnetic structure of intralayer FM and interlayer AFM orderings and monolayer $NiBr_2$ is an intrinsically FM semiconductor, in which the magnetic moment is mainly provided by the *d* orbits of Ni atoms. Furthermore, we find that energies of the interlayer AFM state of AB-stacked bilayer and ABC-stacked trilayer $NiBr_2$ are 7.53 and 10.52 meV/formula unit lower than those of the interlayer FM state, respectively, which means that the interlayer AFM coupling of AB-stacked bilayer and ABC-stacked trilayer $NiBr_2$ are much larger than that of CrI_3 in the high-temperature phase. Meanwhile, it can be seen from the spin-resolved band structure in Figs. 2(a), 2(e), and Figs. 3(a), 3(e) that no matter what interlayer magnetic couplings are FM or AFM, the Fermi level lies within the band gap of bilayer and trilayer $NiBr_2$, thus both of the AB-stacked bilayer and ABC-stacked trilayer $NiBr_2$ are magnetic semiconductors. In contrast, the Fermi energy locates within the conduction bands of bilayer and trilayer $NiBr_2$ in the $Gr/NiBr_2/Gr$ vdW heterostructures, as shown in Figs. 2(b), 2(f), and Figs. 3(b), 3(f). Correspondingly the local densities of states (DOSs) of the $Gr/NiBr_2/Gr$ vdW heterostructures in real space show that when bilayer and trilayer $NiBr_2$ are the interlayer FM state, the minority-spin state of each monolayer of bilayer and trilayer $NiBr_2$ in the vdW heterostructures is metallic, while the majority-spin state of each monolayer $NiBr_2$ is semiconducting, thus the bilayer and trilayer $NiBr_2$ barriers in the vdW heterostructures become half-metal. Moreover, it can be seen from the band structure and local DOSs of the $Gr/NiBr_2/Gr$ vdW heterostructures in Figs. 2 and 3 that when bilayer (trilayer) $NiBr_2$ in the $Gr/NiBr_2/Gr$ vdW heterostructure is the interlayer AFM state, the minority-spin state of Layer 1 (Layer 1 and Layer 3), and the majority-spin state of Layer 2 of bilayer (trilayer) $NiBr_2$ are metallic, while the majority-spin state of Layer 1 (Layer 1 and Layer 3) and the minority-spin state of Layer 2 of bilayer (trilayer) $NiBr_2$ are semiconducting, indicating that the bilayer and trilayer $NiBr_2$ barriers in the vdW heterostructures become half-metal.

In the following, we further understand the half-metallicity of the bilayer (trilayer) $NiBr_2$ barrier in the $Gr/NiBr_2/Gr$ heterostructure. Our calculations show that the calculated electron affinity and ionization energy of isolated bilayer (trilayer) $NiBr_2$ are 5.431 and 6.153 eV (5.452 and 6.157 eV), respectively, while the calculated work function of graphene is 4.245 eV. Since the work function of graphene is smaller than the electron affinity of bilayer (trilayer) $NiBr_2$, the electrons will transfer from graphene to bilayer (trilayer) $NiBr_2$ when they are stacked together to form the $Gr/NiBr_2/Gr$ heterostructure. The band structure and local DOSs of bilayer $NiBr_2$ in Fig. 2 show that the minority-spin conduction bands of each monolayer of bilayer $NiBr_2$ are much closer to the Fermi level than the majority-spin of those in the case of the interlayer FM state of bilayer $NiBr_2$, while the minority-spin conduction bands of Layer 1 and the majority-spin conduction bands of Layer 2 of bilayer $NiBr_2$ are closer to the Fermi level in the case of the interlayer AFM state of bilayer $NiBr_2$. Correspondingly, when bilayer $NiBr_2$ is the interlayer FM state, the electronic transfer from graphene to the minority-spin conduction bands of each monolayer of bilayer $NiBr_2$ in the vdW heterostructure will result in the minority-spin metallic state of each monolayer of bilayer $NiBr_2$ and an upward shift of the Dirac point of graphene away from the Fermi level. In contrast, when $NiBr_2$ is the interlayer AFM state, the electronic transfer from graphene to the minority-spin conduction bands of Layer1 and the majority-spin conduction bands of Layer 2 of bilayer $NiBr_2$ in the vdW heterostructure will lead to the minority-spin metallicity of Layer 1 and the majority-spin metallicity of Layer 2 of bilayer $NiBr_2$, as well as an upward shift of the Dirac point of graphene away from the Fermi level.

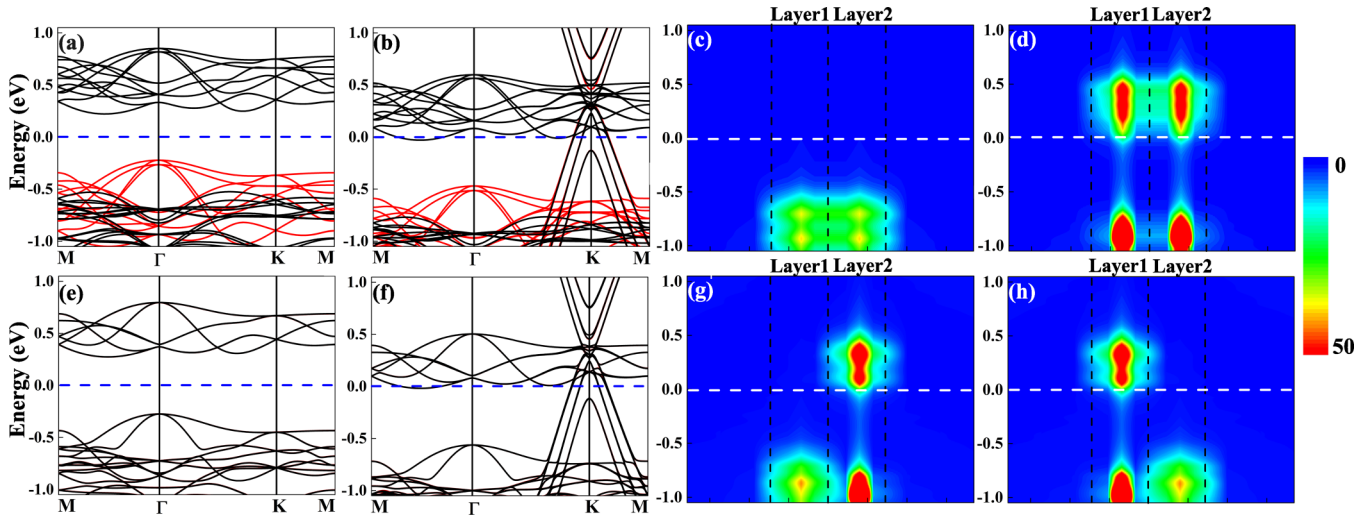

FIG. 2. Band structure of the interlayer (a) FM and (e) AFM bilayer $NiBr_2$. Band structure of the $Gr/NiBr_2/Gr$ heterostructure when bilayer $NiBr_2$ is the interlayer (b) FM and (f) AFM states. Red and black curves represent the majority- and minority-spin bands. Local (c), (g) majority- and (d), (h) minority-spin DOSs in the real space along the transport direction of the $Gr/NiBr_2/Gr$ heterostructure when bilayer $NiBr_2$ is the interlayer (c), (d) FM and (g), (h) AFM states, respectively. The Fermi energy is indicated by the horizontal dashed line.

Similar to bilayer $NiBr_2$ barrier, the electronic transfer from graphene to the minority-spin conduction bands of trilayer $NiBr_2$ barrier will result in the minority-spin metallic state of each monolayer of trilayer $NiBr_2$ and an upward shift of the Dirac point of graphene away from the Fermi level in the case of the interlayer FM state of trilayer $NiBr_2$. Moreover, when $NiBr_2$ is the interlayer AFM state, the electronic transfer from graphene to the majority-spin conduction bands of Layer 2 and the minority-spin conduction bands of Layer 1 and Layer 3 of trilayer $NiBr_2$ barrier will lead to the majority-spin metallicity of Layer 2 and the minority-spin metallicity of Layer 1 and Layer 3 of trilayer $NiBr_2$, as well as an upward shift of the Dirac point of graphene away from the Fermi level. Also, the Bader charge analysis for the $Gr/NiBr_2/Gr$ vdW heterostructure demonstrates that about 0.190 and 0.153 electrons transfer from graphene to bilayer and trilayer $NiBr_2$ in the $Gr/NiBr_2/Gr$ vdW heterostructure. Therefore, the electronic transfer from graphene to the $NiBr_2$ barrier leads to the half-metallicity of the bilayer and trilayer $NiBr_2$ barrier in the $Gr/NiBr_2/Gr$ heterostructure.

C. TMR effect and spin-dependent transport of $Gr/NiBr_2/Gr$ sf-vdW MTJs

The TMR ratio of $Gr/NiBr_2/Gr$ sf-vdW MTJs at zero bias voltage is defined as $\mathrm{TMR} = (G_{\mathrm{FM}} - G_{\mathrm{AFM}})/G_{\mathrm{AFM}} \times 100\%$, where the total conductance $G_{\mathrm{FM}}(G_{\mathrm{AFM}})$ is the summation of major- and minority-spin conductances for the interlayer

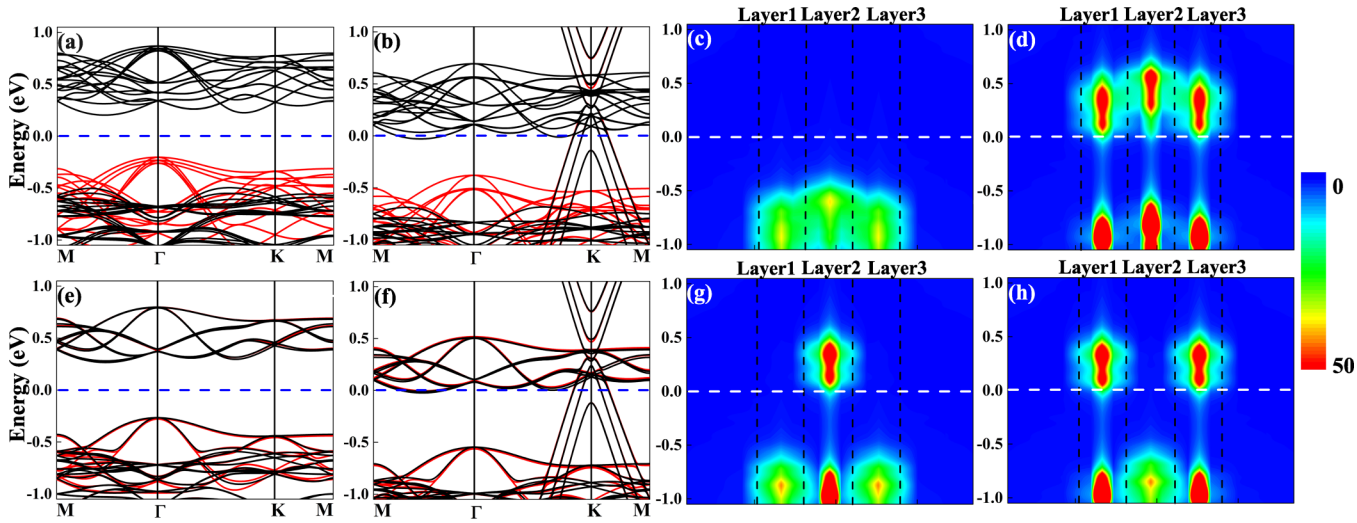

FIG. 3. Band structure of the interlayer (a) FM and (e) AFM trilayer $NiBr_2$. Band structure of the $Gr/NiBr_2/Gr$ heterostructure when trilayer $NiBr_2$ is the interlayer (b) FM and (f) AFM states. Red and black curves represent the majority- and minority-spin bands. Local (c), (g) majority- and (d), (h) minority-spin DOSs in the real space along the transport direction of the $Gr/NiBr_2/Gr$ heterostructure when trilayer $NiBr_2$ is the interlayer (c), (d) FM and (g), (h) AFM states, respectively. The Fermi energy is indicated by the horizontal dashed line.

TABLE I. Calculated conductance (in units of e^2/h) and TMR ratios of $Gr/NiBr_2/Gr$ sf-vdW MTJs with bilayer and trilayer $NiBr_2$ barriers at zero bias voltage. $G_{FM}(G_{AFM})$, $G_{\uparrow FM}(G_{\uparrow AFM})$ and $G_{\downarrow FM}(G_{\downarrow AFM})$ represent the total, major-, and minority-spin conductances for the interlayer FM (AFM) state of the $NiBr_2$ barrier, respectively.

$NiBr_2$	G_{FM}	$G_{\uparrow FM}$	$G_{\downarrow FM}$	G_{AFM}	$G_{\uparrow AFM}$	$G_{\downarrow AFM}$	TMR (%)
Bilayer	3.73×10^{-5}	3.28×10^{-6}	3.40×10^{-5}	1.38×10^{-5}	8.12×10^{-6}	5.66×10^{-6}	170
Trilayer	4.73×10^{-6}	3.59×10^{-8}	4.69×10^{-6}	1.55×10^{-6}	5.82×10^{-7}	9.66×10^{-7}	206

FM (AFM) state of $NiBr_2$ barrier, that is, $G_{FM} = G_{\uparrow FM} + G_{\downarrow FM}(G_{AFM} = G_{\uparrow AFM} + G_{\downarrow AFM})$. Table I lists the calculated conductance and the TMR ratios of the $Gr/NiBr_2/Gr$ sf-vdW MTJs with bilayer and trilayer $NiBr_2$ barriers. It is seen from Table I that the conductance of the $Gr/NiBr_2/Gr$ sf-vdW MTJ with bilayer $NiBr_2$ barrier is much larger than the corresponding one of $Gr/NiBr_2/Gr$ sf-vdW MTJ with trilayer $NiBr_2$ barrier due to the stronger spin-filtering effect of trilayer $NiBr_2$ than that of bilayer $NiBr_2$, and $G_{\downarrow FM}$ of the $Gr/NiBr_2/Gr$ sf-vdW MTJ with bilayer (trilayer) $NiBr_2$ barrier is about one order (two orders) of magnitude larger than $G_{\uparrow FM}$, thus G_{FM} of the $Gr/NiBr_2/Gr$ sf-vdW MTJs are nearly the same as $G_{\downarrow FM}$. Moreover, G_{FM} of the $Gr/NiBr_2/Gr$ sf-vdW MTJ with bilayer (trilayer) $NiBr_2$ barrier is almost two (three) times as large as G_{AFM}. Consequently, the TMR ratios of about 170% and 206% are achieved in the $Gr/NiBr_2/Gr$ sf-vdW MTJs with bilayer and trilayer $NiBr_2$ barriers at zero bias voltage, respectively. As is known, the electron transmission across the $Gr/NiBr_2/Gr$ sf-vdW MTJs is closely related to the intrinsic conduction channels of the graphite electrode and the electronic properties of the $NiBr_2$ barrier. Our calculations show that the conduction channels of the graphite are mainly located at the high-symmetry K points of the 2D BZ. Correspondingly, the electron transmissions across the $Gr/NiBr_2/Gr$ sf-vdW MTJs mainly occur at the K points in all cases because the spin and transverse wave vector $k_{\parallel}$ are conserved in the transmission process. As shown in Figs. 2 and 3, when the $NiBr_2$ barrier is the interlayer FM state, the minority-spin conduction bands of the $NiBr_2$ barrier at the K points are still above the Fermi level although the minority-spin state of the bilayer (trilayer) $NiBr_2$ is metallic, and the minority-spin band gap of the bilayer (trilayer) $NiBr_2$ barrier at the K points is much smaller than the majority-spin one. As a result, the minority-spin transmissions at the K points are much larger than the majority-spin those in the case of the interlayer FM state of $NiBr_2$ barrier, thus $G_{\downarrow FM}$ of the $Gr/NiBr_2/Gr$ sf-vdW MTJ with bilayer (trilayer) $NiBr_2$ barrier is much larger than $G_{\uparrow FM}$.

It is noteworthy that at the optimized biasing voltage, a giant TMR ratio of 10^5% to 10^6% is experimentally achieved in sf-vdW MTJs based on graphite/few-layer CrI_3/graphite vdW heterostructures [26–28]. Therefore, we further investigate the spin-dependent transport and the TMR effect of the $Gr/NiBr_2/Gr$ sf-vdW MTJs at bias voltage. At a bias voltage, the TMR ratio of the $Gr/NiBr_2/Gr$ sf-vdW MTJs is defined as $TMR = (I_{FM} - I_{AFM})/I_{AFM} \times 100\%$, where the total current $I_{FM}(I_{AFM})$ is the summation of major- and minority-spin currents for the interlayer FM (AFM) state of $NiBr_2$ barrier. Figures 4(a) and 4(b) show the bias voltage dependence of the total current across the $Gr/NiBr_2/Gr$ sf-vdW MTJs with bilayer and trilayer $NiBr_2$ in the case of the interlayer FM and AFM states of $NiBr_2$ barrier, respectively. Correspondingly, the TMR ratio as a function of bias voltage for the $Gr/NiBr_2/Gr$ sf-vdW MTJs with bilayer and trilayer $NiBr_2$ are also shown in Figs. 4(a) and 4(b). When bilayer and trilayer $NiBr_2$ are the interlayer FM and AFM states, both I_{FM} and I_{AFM} across the $Gr/NiBr_2/Gr$ sf-vdW MTJs monotonically increase with the increase of bias voltage. It is noteworthy that when the bias voltage is larger than 0.09 V, I_{FM} across the $Gr/NiBr_2/Gr$ sf-vdW MTJ with bilayer $NiBr_2$ barrier rapidly increases with the increase of bias voltage compared to the slow increase of I_{AFM}, while I_{AFM} across the $Gr/NiBr_2/Gr$ sf-vdW MTJ with bilayer $NiBr_2$ barrier significantly increases with the increase of bias voltage when the bias voltage is larger than 0.14 V. Similarly, when the bias voltage is larger than 0.1 V, I_{FM} across the $Gr/NiBr_2/Gr$ sf-vdW MTJ with trilayer $NiBr_2$ barrier rapidly increases with the increase of bias voltage compared to the slow increase of I_{AFM}, while I_{AFM} across the $Gr/NiBr_2/Gr$ sf-vdW MTJ with

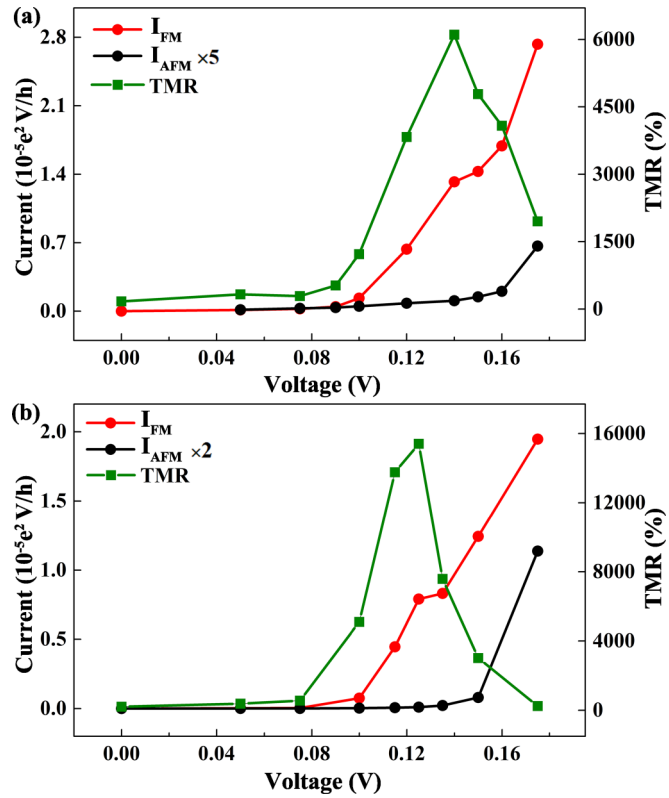

FIG. 4. Total currents of the $Gr/NiBr_2/Gr$ MTJs as a function of bias voltage when (a) bilayer and (b) trilayer $NiBr_2$ are the interlayer FM and AFM states and TMR ratios of the $Gr/NiBr_2/Gr$ MTJs as a function of bias voltage.

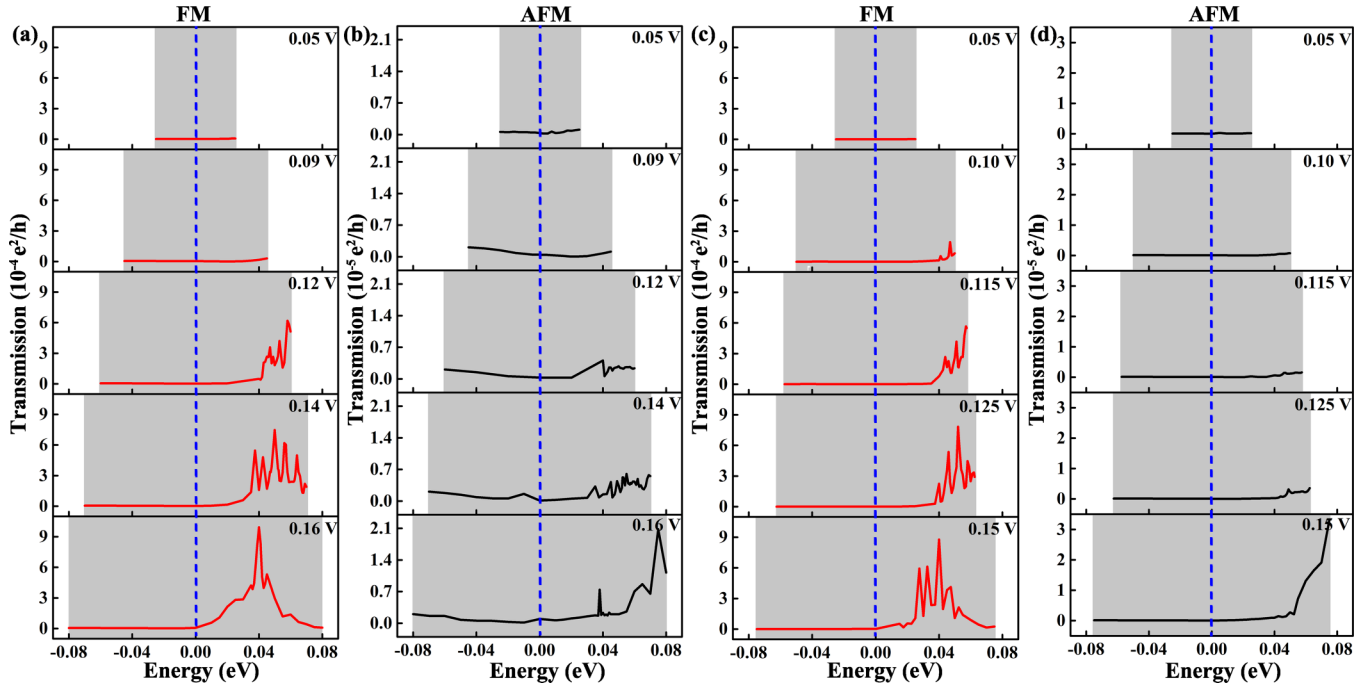

FIG. 5. Total transmission coefficients of the Gr/$NiBr_2$/Gr sf-vdW MTJs with (a), (b) bilayer and (c), (d) trilayer $NiBr_2$ barriers as a function of energy at different bias voltages. Red and black curves represent the transmission coefficients when the bilayer and trilayer $NiBr_2$ barriers are the interlayer FM and AFM states, respectively. The gray shadows represent the bias window. The Fermi energy is indicated by the vertical dashed line.

trilayer $NiBr_2$ barrier significantly increases with the increase of bias voltage when the bias voltage is larger than 0.125 V. Corresponding to above variation of I_{FM} and I_{AFM} with bias voltage, the difference between I_{FM} and I_{AFM} increases first with the increase of bias voltage and then decreases with the further increase of bias voltage. As a result, similar to the experimental results of sf-vdW MTJs formed by a few-layer CrI_3 barrier [25–27], the TMR ratios of the Gr/$NiBr_2$/Gr sf-vdW MTJs with bilayer and trilayer $NiBr_2$ barriers increase first with the increase of bias voltage and then decrease with the further increase of bias voltage after reaching the highest TMR ratio of about 6000% and 14 000%, as shown in Figs. 4(a) and 4(b). Compared to the TMR ratios at zero bias voltage, the TMR ratios of the Gr/$NiBr_2$/Gr sf-vdW MTJs with bilayer and trilayer $NiBr_2$ barriers are increased about 34 and 67 times by bias voltage, respectively.

Equation (2) shows that the currents I_{FM} and I_{AFM} are obtained by integrating transmission coefficients with respect to energies in the bias window, and the energy range of the bias window is from E_F-eV/2 to E_F + eV/2 for a given bias voltage V. Figures 5(a) to 5(d) show the transmission coefficients of the Gr/$NiBr_2$/Gr sf-vdW MTJs with bilayer and trilayer $NiBr_2$ barriers as a function of energy at different bias voltages when the $NiBr_2$ barriers are the interlayer FM and AFM states, respectively. Corresponding to the transmission, Figs. 6(a) to 6(d) show the spin-resolved band structure of the Gr/$NiBr_2$/Gr sf-vdW heterostructures with bilayer and trilayer $NiBr_2$ barriers at different bias voltages in the case of the interlayer FM and AFM state of $NiBr_2$ barrier, respectively. As is mentioned above, the conduction channels of the graphite are mainly located at the K points and the electron transmissions mainly occur at the K points, which means that though there are a couple of bands from $NiBr_2$ crossing the bias window on the left side of the K points, they do not almost contribute to the conductance because the transverse wave vector $k_{\|}$ are conserved in the transmission process. Therefore, we focus on the band structures of the bilayer (trilayer) $NiBr_2$ barriers at the K points to elucidate the electron transport of the Gr/$NiBr_2$/Gr sf-vdW MTJs at bias voltage. It can be seen from Figs. 6(a) to 6(d) that the conduction bands of the bilayer (trilayer) $NiBr_2$ barrier at the K points move towards the Fermi level by increasing bias voltage. Corresponding to the movement of the conduction bands of the bilayer (trilayer) $NiBr_2$ barrier at the K points, the transmission peaks move towards the Fermi level with the increase of bias voltage, as shown in Figs. 5(a) to 5(d). It is noteworthy that when the bias voltage is larger than 0.09 V (0.1 V), the minority-spin conduction bands of the $NiBr_2$ barriers at the K points begin to enter the bias window in the case of the interlayer FM state of bilayer (trilayer) $NiBr_2$, while the conduction bands of the $NiBr_2$ barriers at the K points is still outside the bias window in the case of the interlayer AFM state of bilayer (trilayer) $NiBr_2$. Correspondingly, when the bias voltage is larger than 0.09 V (0.1 V), the transmission peaks enter the bias window in the case of the interlayer FM state of bilayer (trilayer) $NiBr_2$, while the transmission peaks are still outside the bias window in the case of the interlayer AFM state of bilayer (trilayer) $NiBr_2$. Consequently, when the bias voltage is larger than 0.09 V (0.1 V), the integral of transmission coefficients in the bias window increase rapidly with the increase of bias voltage in the case of the interlayer FM state of bilayer (trilayer) $NiBr_2$, resulting in significant increase of I_{FM} across sf-vdW MTJs with the increase of bias voltage. In contrast to significant increase of I_{FM}, the

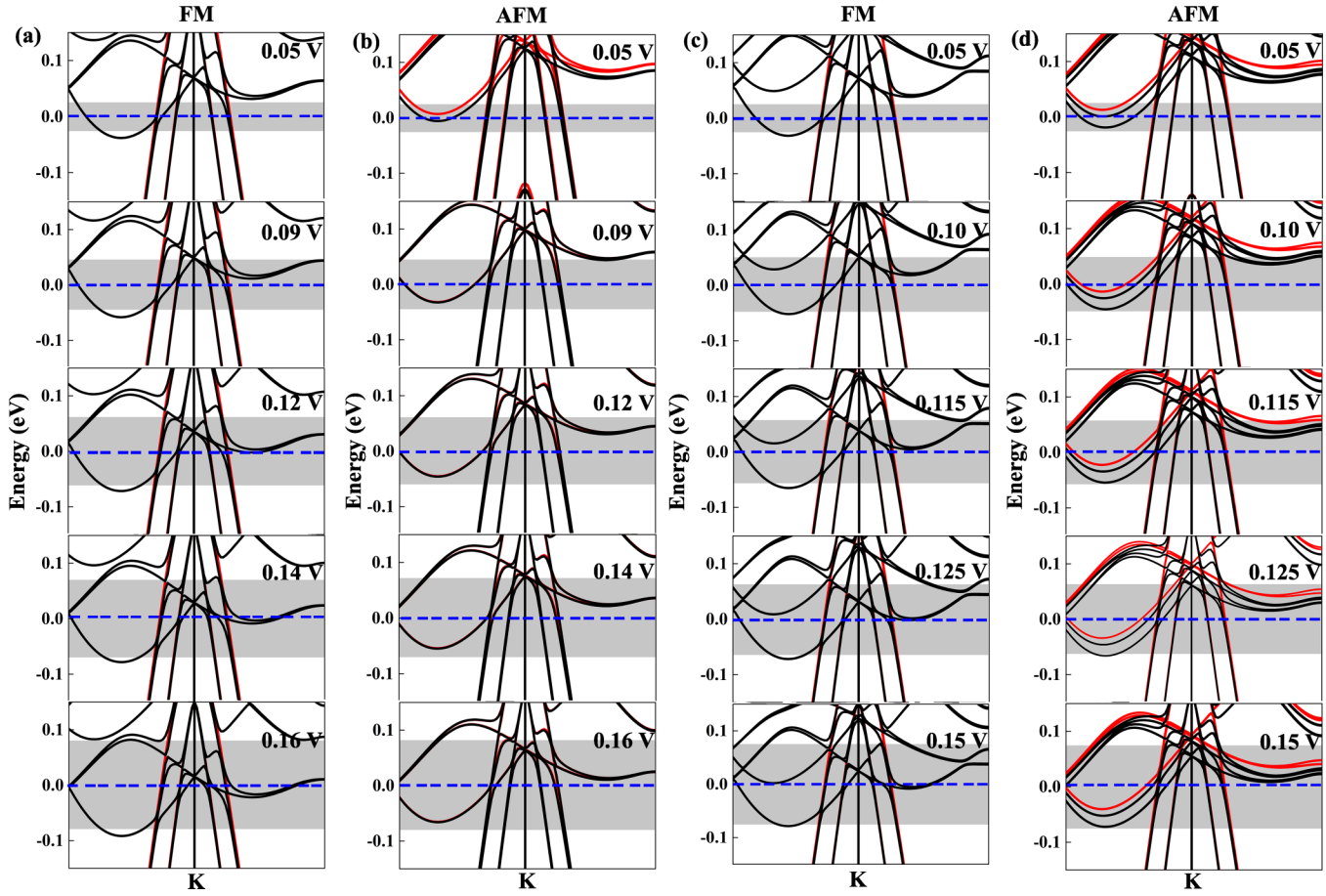

FIG. 6. Band structures around the K points of the $Gr/NiBr_2/Gr$ sf-vdW MTJs with (a), (b) bilayer and (c), (d) trilayer $NiBr_2$ barriers at different bias voltages when bilayer and trilayer $NiBr_2$ are the interlayer (a), (c) FM and (b), (d) AFM states, respectively. The red and black curves represent the majority- and minority-spin bands. The gray shadows represent the bias window. The Fermi energy is indicated by the horizontal dashed line.

integral of transmission coefficients in the bias window, i.e., I_{AFM} increase slowly with the increase of bias voltage when $NiBr_2$ is the interlayer AFM state. Furthermore, when the bias voltage is larger than 0.14 V (0.125 V), the conduction bands of the $NiBr_2$ barriers at the K points also begin to enter the bias window in the case of the interlayer AFM state of bilayer (trilayer) $NiBr_2$, as shown in Figs. 6(b) and 6(d), thus the transmission peaks also enter the bias window. As a result, I_{AFM} across sf-vdW MTJ with bilayer (trilayer) $NiBr_2$ barrier significantly increases with the increase of bias voltage when the bias voltage is larger than 0.14 V (0.125 V).

IV. CONCLUSION

In summary, AB-stacked bilayer and ABC-stacked trilayer $NiBr_2$ are magnetic semiconductors with magnetic structure of intralayer FM and interlayer AFM orderings. It is noteworthy that, similar to the experimental results of sf-vdW MTJs formed by a few-layer CrI_3 barrier, the TMR ratios of the $Gr/NiBr_2/Gr$ sf-vdW MTJs increase first with the increase of bias voltage and decrease with the further increase of bias voltage after reaching the highest points because the conduction bands of the interlayer ferromagnetic (FM) $NiBr_2$ barrier at the K points go into the bias window earlier than those of the interlayer AFM $NiBr_2$ barrier with the increase of bias voltage. Compared to the TMR ratios of about 170% and 206% at zero bias voltage, the TMR ratios of the $Gr/NiBr_2/Gr$ sf-vdW MTJs with bilayer and trilayer $NiBr_2$ barriers are largely increased about 34 and 67 times by the optimized bias voltage, respectively. Correspondingly, a giant TMR ratio of about 6000% and 14 000% can be achieved in the $Gr/NiBr_2/Gr$ sf-vdW MTJs with bilayer and trilayer $NiBr_2$ barriers at 0.14 and 0.125 V bias voltage, respectively. These findings provide promising guidelines for the realization of the high TMR ratio in vdW MTJs.

ACKNOWLEDGMENTS

This work was supported by the National Natural Science Foundation of China (Grant No. 11874173), the National Key Research and Development Program of China (Grant No. 2018YFB0407600), and the Project funded by China Postdoctoral Science Foundation (Grant No. 2020M682897). The authors acknowledge the computational support provided by the High Performance Computing Center of Jilin University and Jilin Province Computing Center.

[1] S. A. Wolf, D. D. Awschalom, R. A. Buhrman, J. M. Daughton, S. von Molnár, M. L. Roukes, A. Y. Chtchelkanova, and D. M. Treger, Science **294**, 1488 (2001).

[2] A. Fert, Angew. Chem. Int. Ed. **47**, 5956 (2008).

[3] E. Y. Tsymbal, O. N. Mryasov, and P. R. LeClair, J. Phys.: Condens. Matter. **15**, R109 (2003).

[4] W. H. Butler, X. G. Zhang, T. C. Schulthess, and J. M. MacLaren, Phys. Rev. B **63**, 054416 (2001).

[5] L. Gao, X. Jiang, S.-H. Yang, J. D. Burton, E. Y. Tsymbal, and S. S. P. Parkin, Phys. Rev. Lett. **99**, 226602 (2007).

[6] F. Bonell, T. Hauet, S. Andrieu, F. Bertran, P. Le Fèvre, L. Calmels, A. Tejeda, F. Montaigne, B. Warot-Fonrose, B. Belhadji, A. Nicolaou, and A. Taleb-Ibrahimi, Phys. Rev. Lett. **108**, 176602 (2012).

[7] W. H. Butler, Sci. Technol. Adv. Mater. **9**, 014106 (2008).

[8] X. Lin, W. Yang, K. L. Wang, and W. Zhao, Nat. Electron. **2**, 274 (2019).

[9] V. P. Ningrum, B. Liu, W. Wang, Y. Yin, Y. Cao, C. Zha, H. Xie, X. Jiang, Y. Sun, S. Qin *et al.*, Research **2020** (2020).

[10] Y. Lee, J. Hayakawa, S. Ikeda, F. Matsukura, and H. Ohno, Appl. Phys. Lett. **90**, 212507 (2007).

[11] S. Ikeda, J. Hayakawa, Y. Ashizawa, Y. Lee, K. Miura, H. Hasegawa, M. Tsunoda, F. Matsukura, and H. Ohno, Appl. Phys. Lett. **93**, 082508 (2008).

[12] K. Masuda, H. Itoh, Y. Sonobe, H. Sukegawa, S. Mitani, and Y. Miura, Phys. Rev. B **103**, 064427 (2021).

[13] B. Huang, G. Clark, E. Navarro-Moratalla, D. R. Klein, R. Cheng, K. L. Seyler, D. Zhong, E. Schmidgall, M. A. McGuire, D. H. Cobden, W. Yao, D. Xiao, P. Jarillo-Herrero, and X. Xu, Nature (London) **546**, 270 (2017).

[14] G. Long, T. Zhang, X. Cai, J. Hu, C.-w. Cho, S. Xu, J. Shen, Z. Wu, T. Han, J. Lin, J. Wang, Y. Cai, R. Lortz, Z. Mao, and N. Wang, ACS Nano **11**, 11330 (2017).

[15] Y. Deng, Y. Yu, Y. Song, J. Zhang, N. Z. Wang, Z. Sun, Y. Yi, Y. Z. Wu, S. Wu, J. Zhu, J. Wang, X. H. Chen, and Y. Zhang, Nature (London) **563**, 94 (2018).

[16] M. Bonilla, S. Kolekar, Y. Ma, H. C. Diaz, V. Kalappattil, R. Das, T. Eggers, H. R. Gutierrez, M.-H. Phan, and M. Batzill, Nat. Nanotechnol. **13**, 289 (2018).

[17] Z. Fei, B. Huang, P. Malinowski, W. Wang, T. Song, J. Sanchez, W. Yao, D. Xiao, X. Zhu, A. F. May, W. Wu, D. H. Cobden, J.-H. Chu, and X. Xu, Nat. Mater. **17**, 778 (2018).

[18] Z. Zhang, J. Shang, C. Jiang, A. Rasmita, W. Gao, and T. Yu, Nano Lett. **19**, 3138 (2019).

[19] X. Li, J. T. Lu, J. Zhang, L. You, Y. Su, and E. Y. Tsymbal, Nano Lett. **19**, 5133 (2019).

[20] Z. Wang, D. Sapkota, T. Taniguchi, K. Watanabe, D. Mandrus, and A. F. Morpurgo, Nano Lett. **18**, 4303 (2018).

[21] H. Lin, F. Yan, C. Hu, Q. Lv, W. Zhu, Z. Wang, Z. Wei, K. Chang, and K. Wang, ACS Appl. Mater. Inter. **12**, 43921 (2020).

[22] D. R. Klein, D. MacNeill, J. L. Lado, D. Soriano, E. Navarro-Moratalla, K. Watanabe, T. Taniguchi, S. Manni, P. Canfield, J. Fernández-Rossier, and P. Jarillo-Herrero, Science **360**, 1218 (2018).

[23] H. H. Kim, B. Yang, S. Tian, C. Li, G.-X. Miao, H. Lei, and A. W. Tsen, Nano Lett. **19**, 5739 (2019).

[24] X. Cai, T. Song, N. P. Wilson, G. Clark, M. He, X. Zhang, T. Taniguchi, K. Watanabe, W. Yao, D. Xiao *et al.*, Nano Lett. **19**, 3993 (2019).

[25] T. Song, M. W.-Y. Tu, C. Carnahan, X. Cai, T. Taniguchi, K. Watanabe, M. A. McGuire, D. H. Cobden, D. Xiao, W. Yao *et al.*, Nano Lett. **19**, 915 (2019).

[26] T. Song, X. Cai, M. W.-Y. Tu, X. Zhang, B. Huang, N. P. Wilson, K. L. Seyler, L. Zhu, T. Taniguchi, K. Watanabe, M. A. McGuire, D. H. Cobden, D. Xiao, W. Yao, and X. Xu, Science **360**, 1214 (2018).

[27] H. H. Kim, B. Yang, T. Patel, F. Sfigakis, C. Li, S. Tian, H. Lei, and A. W. Tsen, Nano Lett. **18**, 4885 (2018).

[28] Z. Wang, I. Gutierrez-Lezama, N. Ubrig, M. Kroner, M. Gibertini, T. Taniguchi, K. Watanabe, A. Imamoglu, E. Giannini, and A. F. Morpurgo, Nat. Commun. **9**, 2516 (2018).

[29] S. Jiang, L. Li, Z. Wang, J. Shan, and K. F. Mak, Nat. Electron. **2**, 159 (2019).

[30] T. R. Paudel and E. Y. Tsymbal, ACS Appl. Mater. Inter. **11**, 15781 (2019).

[31] J. J. Heath, M. Costa, M. Buongiorno-Nardelli, and M. A. Kuroda, Phys. Rev. B **101**, 195439 (2020).

[32] F. Li, B. Yang, Y. Zhu, X. Han, and Y. Yan, Appl. Phys. Lett. **117**, 022412 (2020).

[33] F. Li, B. Yang, Y. Zhu, X. Han, and Y. Yan, Appl. Surf. Sci. **505**, 144648 (2020).

[34] Z. Yan, R. Zhang, X. Dong, S. Qi, and X. Xu, Phys. Chem. Chem. Phys. **22**, 14773 (2020).

[35] N. Sivadas, S. Okamoto, X. Xu, C. J. Fennie, and D. Xiao, Nano Lett. **18**, 7658 (2018).

[36] P. Jiang, C. Wang, D. Chen, Z. Zhong, Z. Yuan, Z.-Y. Lu, and W. Ji, Phys. Rev. B **99**, 144401 (2019).

[37] L. Thiel, Z. Wang, M. A. Tschudin, D. Rohner, I. Gutiérrez-Lezama, N. Ubrig, M. Gibertini, E. Giannini, A. F. Morpurgo, and P. Maletinsky, Science **364**, 973 (2019).

[38] D. Shcherbakov, P. Stepanov, D. Weber, Y. Wang, J. Hu, Y. Zhu, K. Watanabe, T. Taniguchi, Z. Mao, W. Windl *et al.*, Nano Lett. **18**, 4214 (2018).

[39] J. T. Gish, D. Lebedev, T. K. Stanev, S. Jiang, L. Georgopoulos, T. W. Song, G. Lim, E. S. Garvey, L. Valdman, O. Balogun *et al.*, ACS Nano **15**, 10659 (2021).

[40] N. Mounet, M. Gibertini, P. Schwaller, D. Campi, A. Merkys, A. Marrazzo, T. Sohier, I. E. Castelli, A. Cepellotti, G. Pizzi *et al.*, Nat. Nanotechnol. **13**, 246 (2018).

[41] V. V. Kulish and W. Huang, J. Mater. Chem. C **5**, 8734 (2017).

[42] M. A. McGuire, Crystals **7**, 121 (2017).

[43] A. S. Botana and M. R. Norman, Phys. Rev. Mater. **3**, 044001 (2019).

[44] P. Day, A. Dinsdale, E. Krausz, and D. Robbins, J. Phys. C: Solid State Phys. **9**, 2481 (1976).

[45] A. Adam, D. Billerey, C. Terrier, R. Mainard, L. Regnault, J. Rossat-Mignod, and P. Meriel, Solid State Commun. **35**, 1 (1980).

[46] J. Nasser, J. Kiat, and R. Gabilly, Solid State Commun. **82**, 49 (1992).

[47] M. Mushtaq, Y. Zhou, and X. Xiang, RSC Adv. **7**, 22541 (2017).

[48] M. Lu, Q. Yao, C. Xiao, C. Huang, and E. Kan, ACS Omega **4**, 5714 (2019).

[49] M. A. McGuire, H. Dixit, V. R. Cooper, and B. C. Sales, Chem. Mater. **27**, 612 (2015).
[50] H. Liu, X. Wang, J. Wu, Y. Chen, J. Wan, R. Wen, J. Yang, Y. Liu, Z. Song, and L. Xie, ACS Nano **14**, 10544 (2020).
[51] G. Kresse and J. Hafner, Phys. Rev. B **47**, 558 (1993).
[52] G. Kresse and J. Furthmüller, Comput. Mater. Sci. **6**, 15 (1996).
[53] G. Kresse and J. Furthmüller, Phys. Rev. B **54**, 11169 (1996).
[54] P. E. Blochl, Phys. Rev. B **50**, 17953 (1994).
[55] J. P. Perdew, K. Burke, and M. Ernzerhof, Phys. Rev. Lett. **77**, 3865 (1996).
[56] J. Klimes, D. R. Bowler, and A. Michaelides, Phys. Rev. B **83**, 195131 (2011).
[57] J. Taylor, H. Guo, and J. Wang, Phys. Rev. B **63**, 245407 (2001).